Atomic-Layer-Deposition Oxide Nanoglue for Sodium Ion Batteries

Xiaogang Han,[†,⊥] Yang Liu,[‡,⊥] Zheng Jia,[§,⊥] Yu-Chen Chen,[†] Jiayu Wan,[†] Nicholas Weadock,[†] Karen J. Gaskell,[∥] Teng Li,*[,§] and Liangbing Hu*[,†]

[†]Department of Materials Science and Engineering, University of Maryland, College Park, Maryland 20742, United States

[‡]Center for Integrated Nanotechnologies (CINT), Sandia National Laboratories, Albuquerque, New Mexico 87185, United States

[§]Department of Mechanical Engineering and [∥]Department of Chemistry and Biochemistry, University of Maryland, College Park, Maryland 20742, United States

Ⓢ Supporting Information

ABSTRACT: Atomic-layer-deposition (ALD) coatings have been increasingly used to improve battery performance. However, the electrochemical and mechanistic roles remain largely unclear, especially for ALD coatings on electrodes that undergo significant volume changes (up to 100%) during charging/discharging. Here we investigate an anode consisting of tin nanoparticles (SnNPs) with an ALD-Al_2O_3 coating. For the first time, in situ transmission electron microscopy unveiled the dynamic mechanical protection of the ALD-Al_2O_3 coating by coherently deforming with the SnNPs under

the huge volume changes during charging/discharging. Battery tests in coin-cells further showed the ALD-Al_2O_3 coating remarkably boosts the cycling performance of the Sn anodes, comparing with those made of bare SnNPs. Chemomechanical simulations clearly revealed that a bare SnNP debonds and falls off the underlying substrate upon charging, and by contrast the ALD-Al_2O_3 coating, like ion-conductive nanoglue, robustly anchors the SnNP anode to the substrate during charging/discharging, a key to improving battery cycle performance.

KEYWORDS: Nanoglue, atomic-layer-deposition, tin anode, ionic conductivity, Na-ion battery anode, Al_2O_3
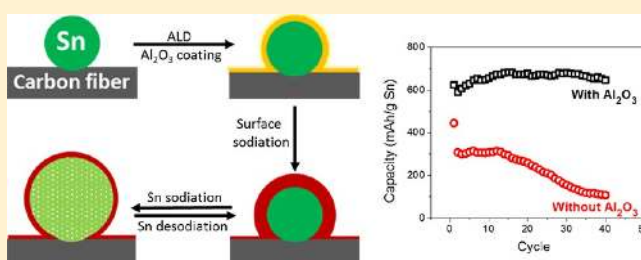
The electrode/electrolyte interface is crucial for electrochemistry behavior and battery performance.[1] Such an interface can often be tuned by surface coatings on the electrode. Compared with the traditional coating approaches,[2−4] atomic-layer-deposition (ALD) enables a precisely controlled ultrathin coating with pinhole free conformal morphology,[5,6] a desirable feature that has led to the increasing application of ALD coatings to improve lithium ion battery (LIB) performance.[7−11] Until now, the majority of the ALD coatings for batteries were applied on cathodes, such as $LiCoO_2$,[12−14] $LiMn_2O_4$,[15] $Li[Li_{0.2}Mn_{0.54}Ni_{0.13}]O_2$,[16] $Li_{1.2}Ni_{0.13}Mn_{0.54}Co_{0.13}O_2$,[17] and so forth, which undergo modest volume changes during charging/discharging. It is believed that the ALD coating on these electrodes behaves like a static physical barrier that separates the electrode from its electrolyte, protecting the electrode active species from dissolving into electrolyte, and preventing side reactions between the electrolyte and electrodes.[18] Research on anodes has been extensively focused on materials with high theoretical specific capacity. However, such anode materials suffer from significant volume change during charging/discharging, which can in turn cause pulverization of the anodes and lead to capacity fading. For example, silicon expands up to 300% in volume upon lithiation forming $Li_{4.4}Si$,[19] and tin experiences up to 420% volume expansion upon sodiation forming $Na_{15}Sn_4$.[20] The behavior of ALD coatings on these anodes experiencing substantial volume

fluctuation during battery cycling remains largely unexplored. It was reported that Si anodes coated with Al_2O_3[21] and TiO_2[22] by ALD can notably improve the performance of lithium ion batteries, but the mechanistic role of such ALD coatings on the Si anodes was not studied.

Meanwhile, room-temperature sodium (Na)-ion batteries (NIBs) are attracting increasing attention due to their promising potential for grid-scale energy storage and the low-cost and natural abundance of sodium resources.[23−26] The cathode materials for NIBs are well-studied, but the development of suitable anode materials remains a grand challenge.[27] Sn is the most promising anode material for NIBs because of its low-cost and outstanding theoretic specific capacity. However, the large volume fluctuation of Sn anodes upon sodiation/desodiation causes high internal stresses, electrode pulverization, and subsequent loss of electrical contact between the active material and current collector, deteriorating the capacity and cyclability. This deleterious impact of volume expansion is even more severe in NIBs than in LIBs, stemming from the 55% larger size of Na ions.[20,28] To date, the reported techniques include the adoption of various Sn/C composite,[29,30] Sn-coated nanoforests,[31] and electrolyte addition.[32]

These tactics achieved improved performance and more understanding of sodium ion storage in Sn anodes, but the performance is still far away from that of practical applications.

In this communication, for the first time we discern how an ALD-Al_2O_3 coating can effectively protect Sn anodes for NIBs from pulverization under severe cyclic deformation during charging/discharging. The anode consists of a hybrid nanostructure of Sn nanoparticles (SnNPs) attached on carbon nanofibers (CNFs), which are then coated with a thin layer of Al_2O_3 by ALD. In situ transmission electron microscopy (TEM) unambiguously reveals that the ALD-Al_2O_3 coating deforms coherently with the SnNPs during the sodiation/desodiation process, offering a synergistically dynamic protection for SnNP anodes under severe sodiation/desodiation-associated volume changes, distinct from the static protection of the ALD coating for cathode materials. Battery tests in coin-cells and ex situ scanning electron microscopy (SEM) proved that the ALD coating remarkably improves the Sn anode structural integrity and battery performance. Chemomechanical modeling of the anode sodiation/desodiation process showed that the ALD-Al_2O_3 coating can, like ion-conductive nanoglue, robustly anchor the SnNPs on the CNF substrate during charging/discharging, retaining the anode's structural integrity that is crucial for battery cycle performance.

Figure 1 schematically explains the mechanistic role of an ALD coating on SnNP anodes in NIBs. The basic anode
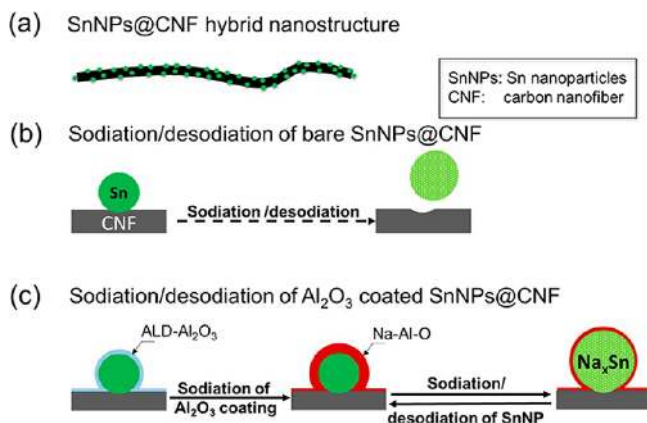

Figure 1. Schematic of the hybrid anode nanostructures and their corresponding sodiation processes. (a) The hybrid nanostructure SnNPs@CNF. (b) During sodiation/desodiation, a bare SnNP debonds from the carbon nanofiber substrate. (c) For the ALD-Al_2O_3 coated SnNPs@CNF, the ALD-Al_2O_3 coating is first uniformly converted to a Na−Al−O layer, followed by the reversible sodiation/desodiation of the SnNP core. Note that the Na−Al−O layer deforms to accommodate the swelling and shrinking of the SnNP core, maintaining the anode structural integrity.

nanostructure of bare SnNPs attached to CNFs, hereafter denoted as SnNPs@CNF, is shown in Figure 1a. For such a basic anode, the SnNPs debond and thus fall off from the underlying CNF substrate after sodiation/desodiation cycles (Figure 1b), resulting in a poor battery performance. By contrast, a 6 nm ALD coating of Al_2O_3 on the basic anode nanostructure, denoted as Al_2O_3/SnNPs@CNF, substantially reinforces the structure via the formation of covalent bonds of Al−O−Sn and Al−O−C between the Al_2O_3 coating and SnNPs@CNF during the ALD treatment. As illustrated in Figure 1c, upon sodiation, the ALD-Al_2O_3 coating is first evenly converted into Na−Al−O, forming an artificial solid electrolyte

interface (SEI) layer. This layer is conductive to sodium ions, allowing for the uniform sodiation of the SnNP core. The conversion of Al_2O_3 coating to form Na−Al−O is irreversible; the SnNP core, however, can be sodiated and desodiated reversibly. During cyclic charging/discharging, the SnNP expands (upon sodiation) and contracts (upon desodiation), accompanied by a conformal swelling and shrinking of the Na−Al−O layer. The synergistic morphology change of the Na−Al−O layer and SnNP core provides a dynamic, mechanical protection for the SnNP anodes, a pivotal mechanism in maintaining the anode's structural integrity and improving battery performance.

The hybrid anode nanostructures were prepared through a sequence of electrospinning, carbonization, and ALD treatment (see Method in Supporting Information). The characterization of the resultant Al_2O_3/SnNPs@CNF is shown in Figure 2. The bright contrast in Figure 2a and Supporting Information Figure S1 indicates a large number of particles dispersed on long, uniform nanofibers. The diameters of the particles and fibers are 180−300 and 280−400 nm, respectively. SEM/energy dispersive X-ray spectroscopy (EDX) element maps in Figure 2b clearly show the nanoparticles are composed of tin and the fibers of carbon. The broad D band (centered at 1330 cm^{-1}) and G band (centered at 1580 cm^{-1}) in the Raman spectrum in Figure 2c suggest amorphous carbon component for the fibers formed from the carbonization of the electrospun polyacrylonitrile (PAN) fabric. The powder X-ray diffraction (XRD) pattern shown in Figure 2d matches the standard pattern of β-Sn (JFPDF: 86-2265) without any significant impurity, which is evidence that the particles are Sn metal. The Al_2O_3 coating is validated from X-ray photoelectron spectroscopy (XPS) and energy-filtered TEM tests (EFTEM). Figure 2e presents the XPS survey scan, high-resolution Al 2p, O 1s regions, and the result of a peak fit for the Sn 3d region. The Al 2p and O 1s regions show single peaks at 74.5 and 531.2 eV, consistent with Al_2O_3.[33] Furthermore, the EFTEM images in Figure 2g display the elements Al and O evenly distribute on the whole structure of SnNPs@CNF, indicating the successful ALD-Al_2O_3 coating. The typical content of Sn is about 26% from thermogravimetric analysis (TGA, Supporting Information Figure S2).

The Sn 3d spectrum, Figure 2e, shows from a peak fit, two pairs of spin−orbit split components. The peaks at 485.6 and 487.5 eV are consistent with Sn in Sn metal (Sn 3d$_{5/2}$) and SnO_2 (Sn 3d$_{5/2}$), respectively. It should be noted that Sn 3d spectra from the bare SnNPs@CNF (not shown here) showed the same two pairs of spin−orbit split components. It indicates a SnO_2 oxidized layer exists on the Sn particle surface. Considering the samples of SnNPs@CNF were exposed in air before ALD treatment, the existence of SnO_2 is reasonable and favorable to the deposition of Al_2O_3 in the ALD process. XPS relative atomic percentage composition data (Supporting Information Table S1) collected for SnNPs@CNF with and without the ALD-Al_2O_3 coating, clearly show that the Al_2O_3 layer sits on top of the Sn nanoparticles because the signal from the Sn is attenuated by ∼25 times by the presence of the Al_2O_3 coating for the as-made structure. It is proved by high-resolution TEM (HRTEM) and fast Fourier transformation (FFT) examinations (Supporting Information Figure S3) that a SnO_2 layer is formed with a thickness estimated to be between 3 and 5 nm. For simplification, the hybrid structures with and without ALD treatment are still denoted as SnNPs@CNF and Al_2O_3/SnNPs@CNF, respectively, omitting the naturally formed SnO_2. Unless otherwise noted, the ALD-Al_2O_3 coating
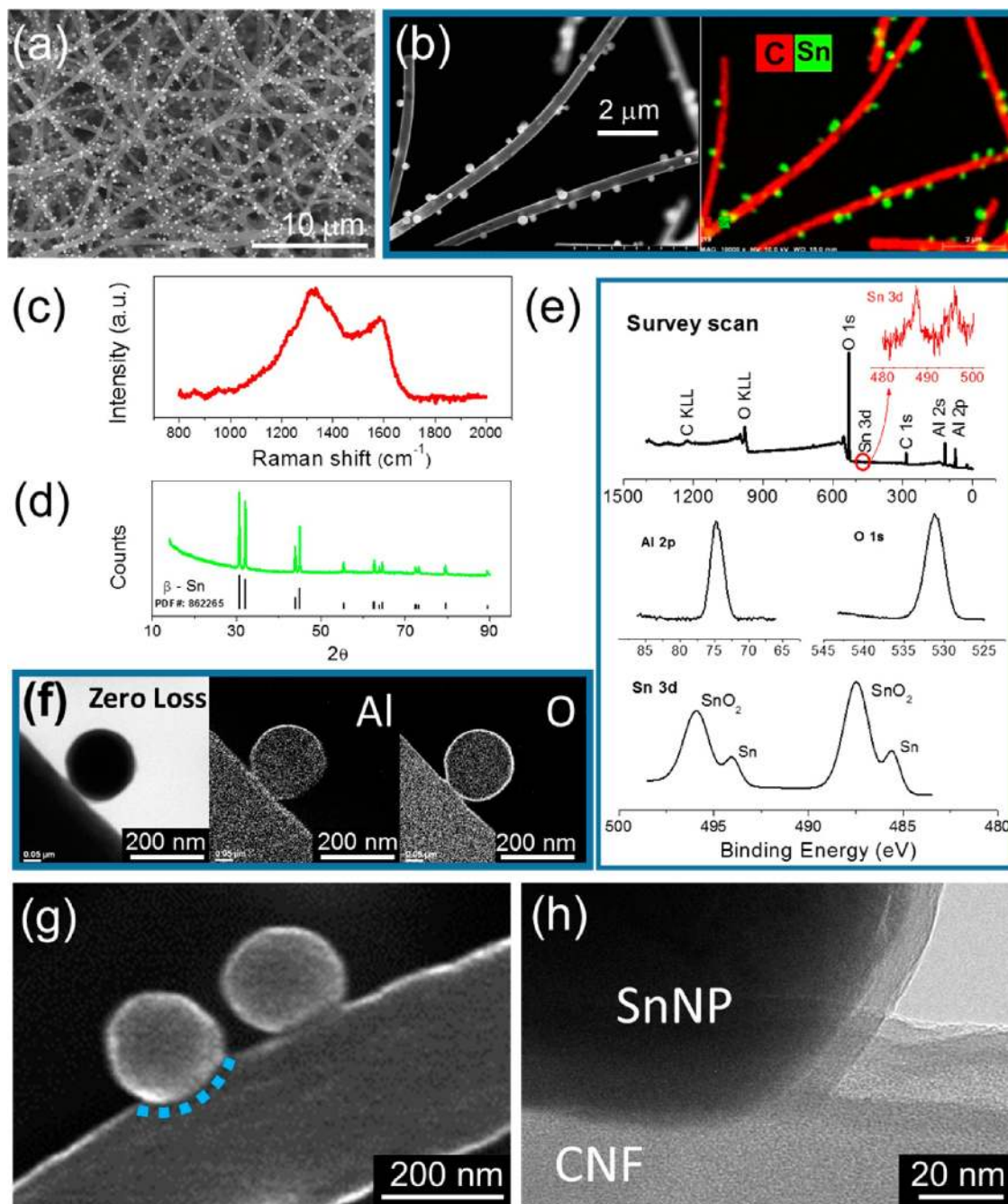
Figure 2. Structure and morphology characterization of as-made Al_2O_3/SnNPs@CNF. (a) Low-magnification SEM image in large area. (b) Element maps of C and O based on SEM energy dispersive X-ray spectroscopy. (c) Micro-Raman scattering. (d) XRD patterns. (e) XPS survey scan, high resolution Al 2p, O 1s regions, and the peak fit for the Sn 3d region. The inset in red is the enlarged Sn 3d region in survey scan. (f) Element distribution of Al and O based on EFTEM mapping (using Al-L edge for Al map and O-K edge for O map) and energy zero-loss image. (g) SEM and (h) TEM images in high magnification to highlight the contact joints between SnNPs and the CNF. The blue dotted curve in (g) indicates the typical craterlike junction.

layer hereinafter includes the Al_2O_3 layer and natural SnO_2 layer (Al_2O_3/SnO_2).

Figure 2g,h highlights the typical contact joints of SnNPs on CNF under high magnification. The SEM image in Figure 2g exhibits the SnNP attached to the CNF within a small craterlike dent. The blue dashed curve on the image marks the crater edge of SnNPs on the CNF. The joint types are associated with SnNP formation from condensation of liquid Sn (see Method in Supporting Information). The close-view TEM image in Figure 2h highlights the joint corner. It distinctly reveals that a

thin, amorphous Al_2O_3 layer wraps the SnNP and extends to the CNF surfaces, forming a solid glue layer at the corner. The Al_2O_3 coating, like a physical nanoglue, reinforces the junctions and improves the electric connection between SnNPs and CNF.

To directly observe the effect of the ALD-Al_2O_3 coating on SnNPs during sodiation/desodiation cycles, in situ TEM electrochemical tests were carried out using the Al_2O_3/SnNPs@CNF as anodes for NIBs. In situ TEM has been a powerful tool to observe the evolution of morphology and
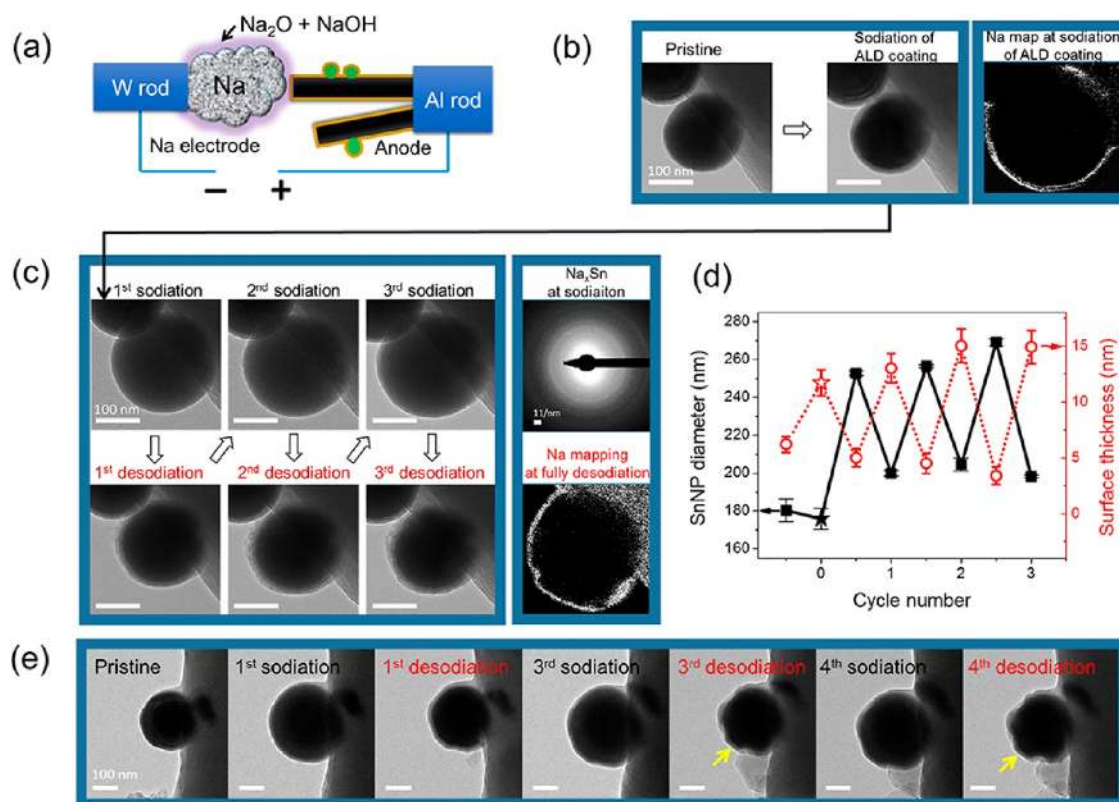
Figure 3. Results of in situ TEM electrochemical sodiation/desodiation cycling. (a) Schematic illustration of the in situ TEM setup. The glowing edge of the Na rod represents the oxidized surface (Na$_2$O and NaOH) serving as solid electrolyte for the nanoscale half-cell. (b,c) In situ TEM images showing the morphology evolution for the Al$_2$O$_3$/SnNPs@CNF anode over operation cycles. (b) The ALD-Al$_2$O$_3$ coating is first converted from the pristine state to a Na−Al−O layer by sodiation. (c) The first three sodiation/desodiation cycles. The corresponding videos for (b,c) can be found in Movies M1−M7 in Supporting Information. The right panel in (b) shows the Na element map after the ALD coating sodiation. The right panel close in (c) shows the SAED pattern at Sn sodiation (top) and the Na map at deep desodiation (bottom) for the Al$_2$O$_3$/SnNPs@CNF anode. (d) Plots the fluctuation of the SnNP size (solid squares) and the Na−Al−O layer thickness (hollow circles) over three sodiation/desodiation cycles. The first data points in each curve refer to the pristine states, and the second points (stars) refer to the sodiation of the ALD coating into a Na−Al−O layer. The data points are linked with lines as a guide for eyes, and all the error bars indicate the variation from three measurements. (e) In situ TEM images showing the 1st, 3rd, and 4th cycle for the control SnNPs@CNF anode (without Al$_2$O$_3$ coating) during sodiation/desodiation cycles. The yellow arrows highlight the rugged surface of the SnNP after operation cycles. All the scale bars are 100 nm. More details can be found in Movies M1−M7 in Supporting Information.

electrochemical reaction in nanobattery electrodes during charging/discharging in real-time.[34−37] Figure 3a schematically illustrates the in situ TEM setup for the half-cell of Na ion nanobatteries. Briefly, the cell is built by driving the Na electrode with a naturally formed solid electrolyte of Na$_2$O and NaOH on surface to connect the carbon fiber of the anode. Upon initial sodiation, as shown in Figure 3b and in situ Movie M1 (see Supporting Information), the ALD-Al$_2$O$_3$ coating expands first before the sodiation of the SnNP core. Figure 3b shows that the ALD-Al$_2$O$_3$ coating thickness increases from 6.2 to 11.7 nm, while the SnNP core almost keeps its original size of 180 nm (subtracting the Al$_2$O$_3$ layer thickness). This is further confirmed by the corresponding Na mapping image (using Na-L edge, right panel to Figure 3b) in which Na is evenly distributed in the sodiated ALD coating.

As shown in Movies M1 and M2 (Supporting Information), the SnNP core expands (sodiates) immediately after the full sodiation of the ALD coating. The first three cycles of SnNP sodiation/desodiation were recorded in Movies M2-M7 (Supporting Information), which unambiguously reveal the morphology evolution of the ALD coating on the SnNPs during the charging/discharging cycles. Figure 3c presents the TEM images of the Al$_2$O$_3$/SnNPs@CNF at maximum

sodiation and desodiation states during these three cycles. In the three sodiation states (upper row in Figure 3c), the SnNP is uniformly expanded to 253, 257, and 269 nm (also see Figure 3d), corresponding to about 178, 191, and 233% volume expansion, respectively. For all three cycles, the expansion is less than the theoretical limit of 420% by forming a crystalline Na$_{15}$Sn$_4$ phase.[35] The selected-area electron diffraction (SAED) pattern at the upper right in Figure 3c proves the sodiation states are in an amorphous phase (Na$_x$Sn, $x < 3.75$). Evidently, the Sn particle is not fully sodiated in our experiments, likely due to the limitations of the in situ TEM electrochemistry system. In the three desodiation states (bottom row in Figure 3c), the SnNP uniformly contracts to 200, 205, and 198 nm (also see Figure 3d) from the corresponding sodiation states, respectively. The volume of the SnNP after deep desodiation in these three cycles is still about 37, 48, and 33% greater than the original volume, respectively. The discrepancy is caused by an irreversible change in particle shape and volume during the cycling.[30,38] The Na mapping image at the bottom right of Figure 3c clearly shows that Na still remains within the ALD layer in a similar sample at deep desodiated states. It suggests that the surface irreversibly converts to a stable Na-containing layer once sodiated from the pristine Al$_2$O$_3$/SnO$_2$. Considering

D

dx.doi.org/10.1021/nl4035626 | Nano Lett. XXXX, XXX, XXX−XXX
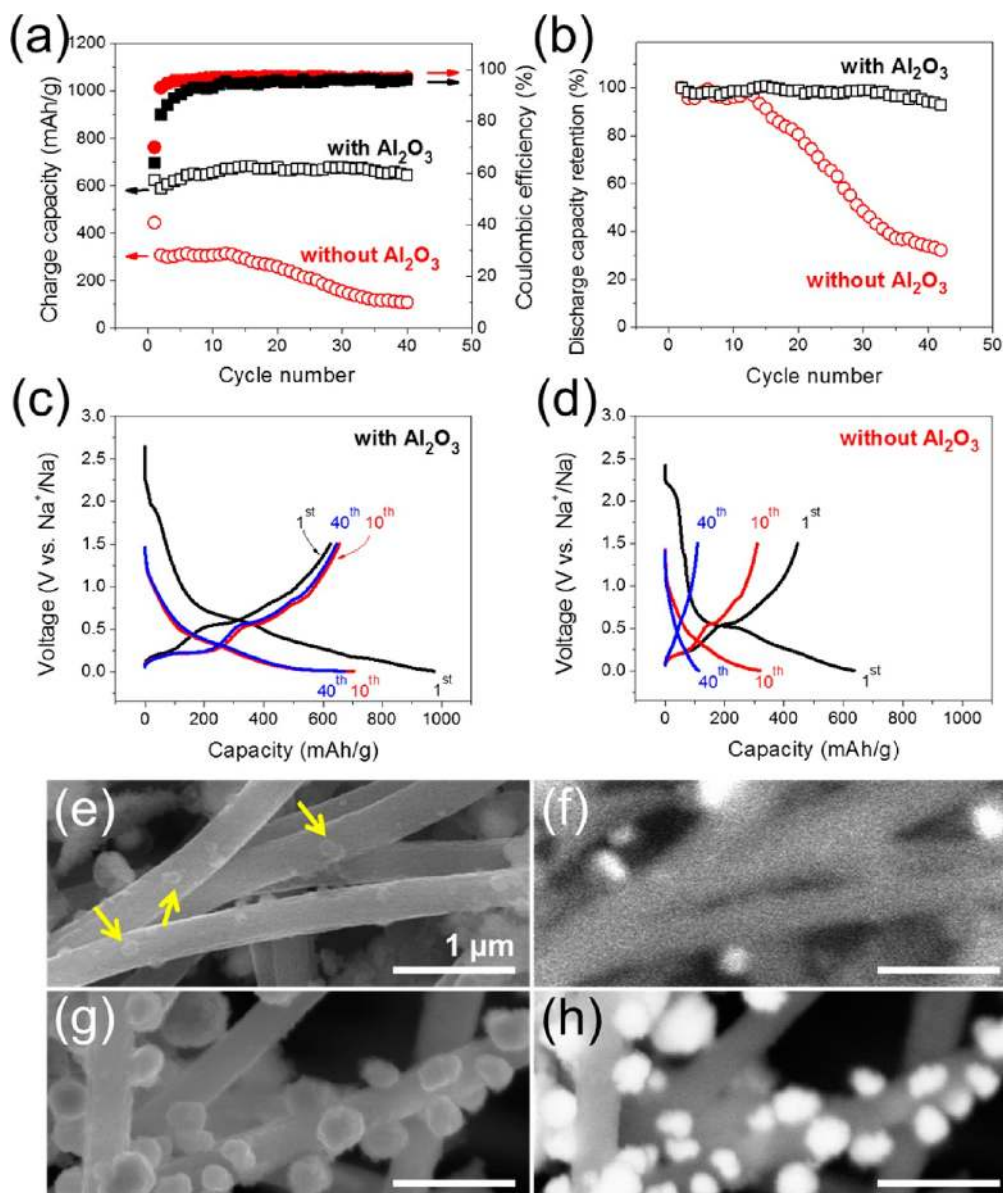
Figure 4. Results of coin-cell electrochemical tests and ex situ SEM. (a–d) Comparison of battery performance using SnNPs@CNF anodes with and without an ALD-Al_2O_3 coating in half-cell for NIBs: (a) Discharge/charge cycle performance and Coulombic efficiency. (b) Discharge capacity retention. (c,d) Voltage profiles of the 1st, 10th, and 40th cycle. (e–h) Ex situ SEM images for the anodes without (e,f) and with (g,h) ALD-Al_2O_3 coating disassembled from the coin-cell battery after 40 cycles. The SEM images in (e,g) are recorded with the secondary electron (SE) detector, and those in (f,h) are recorded with the backscattered electron (BSE) detector. The yellow arrows in (e) indicate the traces of fallen SnNPs left on carbon fibers. The scale bars in (e–h) are 1 μm.

Al_2O_3 and SnO_2 irreversibly convert to Li–Al–O,[39,40] Li_2O, and Sn[41] upon initial electrochemical lithiation, the Al_2O_3/SnO_2 layer in our experiments is likely to convert to Na–Al–O, Na_2O, and Sn. Because the produced Sn of negligible amount is the same material as the core, the sodiated ALD coating is simply denoted as the Na–Al–O layer.

Such a Na–Al–O layer, as demonstrated in Movies M2–M7 (Supporting Information), shows remarkable reversible stretchability during charging/discharging cycles. Similar to the inflation/deflation of a balloon, the Na–Al–O layer thins when the SnNP expands upon sodiation and thickens when the SnNP contracts upon desodiation. During the three sodiation/desodiation cycles, the layer thickness, almost reversibly changed between an average of 4.3 and 14.3 nm (Figure 3d) with its surface area periodically swelling by an average of 67%

calculated from the SnNP core expansion (Supporting Information Figure S4). When compared to the original Al_2O_3 coating before cycling, the surface area of Al_2O_3 increased by 108%. The complementary fluctuation of the Na–Al–O layer thickness, surface area, and the SnNP core size over the cycles are further plotted in Figure 3d and Supporting Information Figure S4.

The homogeneous change of the Na–Al–O surface area without any noticeable fractures suggests a reversible, stretchable glue effect of the Na–Al–O layer, a crucial feature that enables the coherent conformation between the Na–Al–O layer and the SnNP during substantial volume fluctuation in charging/discharging cycles. Such a synergistic action between the Na–Al–O layer and the SnNP core effectively provides a dynamic mechanical protection for the Sn electrodes during

operation cycles. It was reported that SnNPs of about 10 nm are not sufficiently small to prevent pulverization during electrochemical lithiation/delithiation.[42,43] However, pulverization of the SnNPs and the delamination of the Na−Al−O layer do not appear in the in situ cycling tests. In other words, the dynamic protection of the ALD coating significantly enhances the electrode integrity. This observation is distinctly different from the behavior of the conformal copper coating on silicon nanowire by chemical vapor deposition (CVD), in which the copper fractured as the nanowire expanded.[44] Furthermore, Supporting Information Movies M2−M7 show that during sodiation/desodiation, the deformation of both the Na−Al−O layer and the SnNP is isotropic, and the Na−Al−O layer surface and the SnNP surface are rather smooth. This implies that Na ions are uniformly intercalated/deintercalated through the stable Na−Al−O layer, which serves as a Na ion buffer. It should be mentioned that the composition of the formed Na−Al−O layer is not known under our current experimental setup. However, a thermodynamically stable phase is reached after sodiation, as similar with the lithiation of Al_2O_3.[40] Future experiments and simulations can help to understand the composition and phase of the Na−Al−O layer.

To further confirm the mechanistic role of the ALD-Al_2O_3 coating, the control anode without an ALD coating (SnNPs@CNF) is tested using in situ TEM. The results are shown in Figure 3e. Distinct from the isotropic nature of the deformation of Al_2O_3/SnNPs@CNF during operation cycles, the surface of the bare SnNP becomes rough after the first sodiation/desodiation cycle and further roughens in the third and fourth cycles. The rugged surface of the SnNP after cycling, as highlighted by the yellow arrows in Figure 3e, could facilitate the initiation of SnNP debonding from CNF, leading to the SnNP falling off and further pulverization. So far, no quantitative or even qualitative data about the mechanical properties of nanosized Na−Al−O have been reported. From our experimental testing and chemomechanical simulation, we can summarize the characteristics of Na−Al−O's deformation as follows. (1) In the in situ TEM observation, we do see the Na−Al−O coating survives at least ∼30% tensile strain without fracture. This experimental observation reveals that in contrast to the brittle and stiff nanosized Al_2O_3, which can only sustain ∼5% tensile strain, the Na−Al−O coating is very ductile. (2) As a metal alloy/oxide that can survive ∼30% tensile strain, we believe Na−Al−O should have a linear elastic deformation behavior at small strain level followed by a plastic deformation behavior at large strain level. (3) As a result of sodiation, the elastic modulus of Na−Al−O must be smaller than that of Al_2O_3. The above comparison between the two types of anode nanostructures clearly demonstrates that the ALD-Al_2O_3 coating (and its sodiated counterpart, the Na−Al−O layer) plays a crucial role in stabilizing the large deformation of the anode nanostructure upon sodiation/desodiation, maintaining the electrode structural integrity during operation cycles.

To further demonstrate the impact of the dynamic mechanical protection from the ALD nanoglue coating, the Al_2O_3/SnNPs@CNF samples are tested as anodes in half-cells. The batteries are tested in coin-cells employing organic liquid electrolyte, as opposed to the Na_2O and NaOH solid electrolyte in in situ TEM electrochemical tests. For comparison, the control anodes of SnNPs@CNF are also tested under the same conditions. Figure 4 compares the results of both battery performance and ex situ SEM observation. Figure 4a clearly shows that the ALD-treated anodes deliver an

initial charge capacity of 625 mAh/g, which decreases modestly at the second cycle, and then stabilizes at 650 mAh/g for the next 40 cycles. By contrast, the anodes without any ALD treatment show a low initial charge capacity of 445 mAh/g. After 13 stable cycles at 310 mAh/g, the capacity rapidly decays, reaching 110 mAh/g at the 40th cycle. All specific capacities presented here are calculated based on the Sn mass less any contribution from the carbon (Supporting Information Figure S5). Obviously, the ALD-treated anodes delivers almost twice the reversible specific capacity as the untreated counterparts. Though we did not know the explicit reason, we believe that the electrolyte solution deteriorates the electrical and physical connection between the SnNPs and CNF, and thus reduces the active material effective mass. In the case of Al_2O_3/SnNPs@CNF, the ALD-Al_2O_3 coating physically protects the electrode structural integrity, and thus maintains the electrode material active. The improved performance is better than the best one for NIBs so far in which is reported an initial capacity of 722 mAh/g along with <500 mAh/g retained after 40 deep cycles.[30]

Figure 4b compares the discharge specific capacity retention. The Al_2O_3/SnNPs@CNF anode is rather stable and retains 93% of its initial discharge capacity at the 40th cycle. In a sharp contrast, the discharge capacity of the control anode SnNPs@CNF decreases quickly down to 32% of its initial value at the 40th cycle. The voltage profiles at the first, 10th, and 40th cycle are given in Figure 4c,d for the Al_2O_3/SnNPs@CNF and SnNPs@CNF anodes, respectively. For the first and 10th discharge/charge curves, both anodes clearly exhibit four plateaus at about 0.2, 0.28, 0.55, and 0.83 V, corresponding to $Na_{15}Sn_4$, Na_9Sn_4, NaSn, and $NaSn_5$, respectively.[28] However, the 40th curves are essentially different for the two anodes. For the anode with the ALD coating, the 40th profile displays all four plateaus of the Sn−Na reaction, almost identical with the 10th profile, indicating the Sn anode is still active. However, for the anode without ALD coating, the 40th profile just shows a few weak plateaus (also see Supporting Information Figure S6), implying the Sn anode has degraded significantly.

To further confirm that the improvement of battery performance is related to ALD-Al_2O_3 coating, ex situ SEM was performed for both anodes after 40 charging/discharging cycles. The disassembled anodes were immersed in fresh electrolyte overnight, then gently rinsed with acetone and acetonitrile several times. Figure 4e reveals that for the anodes without ALD coating, the majority of the carbon fibers are bare with craters corresponding to the initial locations (yellow arrows) of the SnNPs. Figure 4f shows the corresponding backscattered electron (BSE) image in which the uniform contrast of the CNF surface confirms that no different phase exists where the craters stand, and the bright spots are a few of the fallen SnNPs. The falling-off of the SnNPs from the CNF substrate leads to the loss of contact with the current collector, thus accounting for the low capacity and poor cyclability of the tested NIBs. By contrast, as shown in the SEM image and the corresponding BSE image in Figure 4g,h, respectively, the SnNPs in the Al_2O_3/SnNPs@CNF anode remain securely glued to the CNF substrate after 40 cycles.

From the good battery characterization in coin-cells and in situ TEM observations, the ALD-Al_2O_3 coating not only reinforces the structure integrity but also provides Na ion conductive path that is created from the irreversible conversion to Na−Al−O. The irreversible conversion is reflected in cyclic voltammetry (CV) profile of the Al_2O_3/SnNPs@CNF anodes
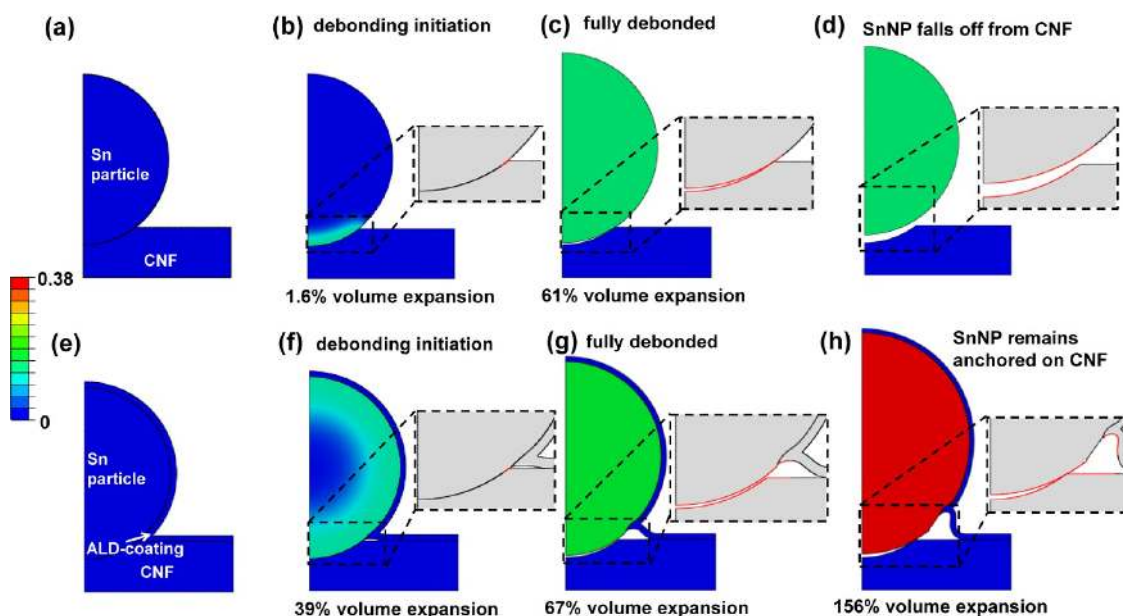
Figure 5. FEM modeling of sodiation in SnNP. (a) The original SnNP@CNF structure. (b−d) Sodiation process of SnNP@CNF anode. Color contour denotes the normalized sodium concentration. Insets show the bonding and debonding state along the SnNP/CNF interface; red represents interface debonding while black represents region still bonded. As sodiation proceeds, the Sn particle completely falls off from the CNF due to the large volume expansion (61%). (e) The original Al_2O_3/SnNPs@CNF structure. (f−h) Sodiation process of the ALD-Al_2O_3/SnNP@CNF structure. ALD-Al_2O_3 is sodiated quickly and irreversibly and therefore serves as sodium reservoir in following sodiation/desodiation cycles. Because of the mechanical constraint of the ALD coating, the initiation of interface debonding is significantly retarded to a later sodiation stage corresponding to 39% volume expansion. Even though the SnNP/CNF interface is fully debonded at 67% volume expansion, the mechanically durable Na−Al−O layer allows further sodiation of the SnNP and effectively anchors the particle on the CNF, preventing capacity fading.

in coin-cells (Supporting Information Figure S7). As shown in Supporting Information Figure S7a, the magnitude of the reduction current is much higher than the oxidation current, and between 1.2 and 0 V the reduction current manifests as a broad bump with a sawtooth-like contour at early cycles. This behavior implies various complicated reductions at the electrode surfaces. The reduction current gradually decrease with cycling and at the sixth cycle the sawtooth disappears. In the oxidation curves, however, there are no corresponding oxidation components with significant oxidation current. Oxidation peaks presented at 0.24, 0.29, 0.6, and 0.83 V are nearly identical with the four plateau potentials in the galvanostatic charge/discharge curves. This is consistent with the observation in in situ TEM that the Al_2O_3 coating is sodiated irreversibly in the first charge stage. To further confirm this conclusion, CV testing is also performed on a control SnNPs@CNF anode. The first cycle is shown in Supporting Information Figure S7b, and clearly no sawtooth-like curves are found. The broad peak at about 0.6 V is attributed to the formation of a solid electrolyte interphase (SEI).[45]

To decipher the glue effect of the ALD-Al_2O_3 coating for the SnNP anode, chemomechanical simulations compare the sodiation/desodiation process of a bare SnNP/CNF with that of Al_2O_3/SnNP@CNF. Figure 5a−d shows snapshots of the bare SnNP@CNF at various stages during the sodiation half-cycle (also see Movies M8−M11 in Supporting Information). The pristine bare SnNP is initially bonded to the underlying CNF via a cohesive interface, through which Na ions are transported into the SnNP (Figure 5a). The SnNP undergoes a two-stage sodiation process during the charging half-cycle.[40] In the first stage, the sodiation front advances via the migration of a sharp phase boundary separating the pristine Sn phase and an amorphous intermediate Na_xSn ($x \sim 0.5$) phase (Figure 5b). In

the second stage, after the sharp sodiation reaction front sweeps through the whole SnNP, the particle is then further sodiated to several Na-rich phases without an appreciable reaction interface (Figure 5c,d). During the sodiation process, the Sn particle expands in volume to accommodate the insertion of Na ions. The accumulation of volume expansion concentrates a stress at the SnNP/CNF interface, initiating particles debonding along the interface. As illustrated in the inset of Figure 5b, the interfacial debonding (indicated by the red color) initiates at the edge of the SnNP/CNF interface only when the overall volume expansion is 1.6%. As sodiation progresses the SnNP volume continues to increase, which causes further propagation of the interfacial debonding (Supporting Information Figure S8). At an overall volume expansion of 61%, the debonding front reaches the bottom of the SnNP/CNF interface (Figure 5c). After that, the SnNP is fully detached from the CNF (Figure 5d, Supporting Information Movies M8 and M9) and loses contact with the current collector. It is worth noting that in the in situ electrochemical TEM experiment the SnNP did not fall off, which is likely due to the van der Waals force in the TEM vacuum system. In the coin-cell system, the SnNPs are immersed in a liquid electrolyte and can easily drift away from the CNF. Experimentally, Na ions are possibly inserted into the SnNPs through the whole outer surface in coin-cell with liquid electrolyte, rather than solely diffusing through the SnNP/CNF interface. Simulations of this case (Supporting Information Figure S10) also result in similar interfacial debonding and falling off of the SnNP from the CNF. This is the major reason for the capacity fading and associated cycling performance degradation of the NIB observed in the experiments (Figure 4a,b).

By contrast, simulations of the SnNP with ALD-Al_2O_3 coatings clearly illustrate the glue effect of the ALD coating

that robustly anchors the SnNP on the CNF during sodiation/desodiation process. Figure 5e−h plots snapshots of the ALD-coated SnNP at various sodiation stages. As the charging half-cycle begins, the ALD-Al_2O_3 coating is first converted to a Na−Al−O layer, which in turn serves as the ion-conducting channel. In this case, Na ions diffuse into the SnNP through the entire surface. Such a whole-surface sodiation leads to an unsodiated pristine Sn core wrapped by a Na_xSn ($x \sim 0.5$) annulus (Figure 5f) in the first sodiation stage. While the SnNP expands as sodiation progresses, the Na−Al−O layer deforms coherently with the SnNP, providing a strong mechanical constraint that effectively retards the initiation of SnNP/CNF interfacial debonding to an overall volume expansion of 39% (Figure 5f), compared with 1.6% in the case of the bare SnNP. At a volume expansion of 67% of the SnNP, the whole SnNP/CNF interface is debonded (Figure 5g). However, the sodiated SnNP is still securely wrapped by the mechanically durable Na−Al−O layer and thus can be further sodiated to an even larger volume. Upon desodiation, the SnNP shrinks and the mechanical constraint from the Na−Al−O layer keeps the SnNP anchored on the CNF (Supporting Information Figure S9 and also Movies M10 and M11) without losing capacity. This ionic conductive glue effect explains the remarkably high initial capacity and high capacity retention of ALD-coated SnNP anodes shown in Figure 4a,b.

The correlation between the mechanical and electrochemical properties of the anodes with the thickness of Al_2O_3 coating can be estimated from mechanics and chemistry. From our mechanical simulations, we know that a thin ALD coating (e.g., with 5 nm thickness) can only provide limited mechanical constraints to the Sn particle. Thus the coating is not strong enough to prevent the interfacial debonding induced by large volume changes. As shown in Supporting Information Figure S11a, at 56% volume expansion the Sn particle is fully detached from its underlying substrate (delamination is represented by the red color along the interface shown in the inset). In contrast, interface of SnNP/CNF is only partially debonded in the case with 10 nm thick ALD coating (Supporting Information Figure S11b). In contrast, a 40 nm thick ALD coating (Supporting Information Figure S11c) fully prevents interfacial delamination at the same volume expansion level. This is because a thick ALD coating strongly constrains the deformation of an SnNP. Supporting Information Figure S11a−c indicates that compared with thinner ones thicker ALD coatings provide stronger mechanical protection to the underlying Sn particle and therefore the Sn particle is less prone to detach from the CNF substrate. In Supporting Information Figure S11d, the Von-mises stress level along the thickness direction of the ALD coating is recorded for different coating thicknesses. The plot indicates a higher stress level for thinner ALD coatings. The high stress level accumulated in the thin ALD coating may fracture the coating itself and let the debonded particle escape. From a mechanical point of view, therefore, a thicker ALD coating provides a better protection effect.

From the electrochemistry point of view, the increase of the Al_2O_3 coating thickness does not facilitate the first Coulombic efficiency (Qe). From observations in in situ TEM and electrochemical CV, the surface layer irreversibly consumes Na ions to form the Na−Al−O structure. A thicker Al_2O_3 coating will consume more cathode material (sodium ions) leading to a lower Qe. We examined the effect of a 6 and 15 nm Al_2O_3 coating on SnNPs@CNF anodes in half-cells and measured the

first Qe of 64 and 46%, respectively. Additionally, increasing the Al_2O_3 coating thickness will reduce the electronic and ionic conductivity. As shown in Supporting Information Figure S12, the impedance of SnNPs@CNF with a 15 nm ALD-Al_2O_3 coating is much higher than that of 6 nm ALD-Al_2O_3 coating before charge/discharge cycling. Though the ionic conductivity of the coating layer may remarkably improve after converting to Na−Al−O, the thicker Na−Al−O layer may have higher impedance. Finally, thicker Al_2O_3 coatings will reduce the specific capacity of the anode. From the combination of mechanical and electrochemical considerations with regards to the coating thickness, there is a thickness which optimizes first Qe, specific capacity and cycling performance.

In summary, our complementary experiments and simulations reveal three novel features of the stretchable ion-conductive glue effect of an ALD coating for SnNPs@CNF anodes. First, the ALD-Al_2O_3 coating and SnO_2 layer reacts with Na ions to irreversibly form a Na−Al−O layer. This newly formed Na−Al−O layer acts as an ion transport channel and improves Na ions diffusion into the SnNP through its whole surface. Second, the strong mechanical constraint from the Na−Al−O layer drastically enhances the durability of the SnNP/CNF interface by increasing the critical volume expansion for debonding initiation from 1.6 to 39%. Last, but most critically, the mechanically durable Na−Al−O layer effectively anchors the SnNPs on the CNF during the severe volume changes under charging/discharging, the key mechanism to protect the anode from capacity fading during operation cycles.

■ ASSOCIATED CONTENT

Ⓢ Supporting Information

Detail of experimental and additional figures and tables depicting experiment results. This material is available free of charge via the Internet at http://pubs.acs.org.

■ AUTHOR INFORMATION

Corresponding Authors

*E-mail: (L. H.) binghu@umd.edu.
*E-mail: (T. L.) LiT@umd.edu.

Author Contributions

[⊥]X.H., Y.L., and Z.J. contributed equally to this work.

Notes

The authors declare no competing financial interest.

■ ACKNOWLEDGMENTS

H

dx.doi.org/10.1021/nl4035626 | Nano Lett. XXXX, XXX, XXX−XXX

■ REFERENCES

(1) Jung, Y. S.; Cavanagh, A. S.; Gedvilas, L.; Widjonarko, N. E.; Scott, I. D.; Lee, S.-H.; Kim, G.-H.; George, S. M.; Dillon, A. C. *Adv. Energy Mater.* **2012**, *2* (8), 1022−1027.

(2) Li, C.; Zhang, H. P.; Fu, L. J.; Liu, H.; Wu, Y. P.; Rahm, E.; Holze, R.; Wu, H. Q. *Electrochim. Acta* **2006**, *51* (19), 3872−3883.

(3) Liu, J.; Meng, X.; Banis, M. N.; Cai, M.; Li, R.; Sun, X. *J. Phys. Chem. C* **2012**, *116* (27), 14656−14664.

(4) Wu, H.; Yu, G.; Pan, L.; Liu, N.; McDowell, M. T.; Bao, Z.; Cui, Y. *Nat. Commun.* **2013**, *4*, 1943.

(5) Knez, M.; Niesch, K.; Niinistoe, L. *Adv. Mater.* **2007**, *19* (21), 3425−3438.

(6) George, S. M. *Chem. Rev.* **2009**, *110* (1), 111−131.

(7) Detavernier, C.; Dendooven, J.; Sree, S. P.; Ludwig, K. F.; Martens, J. A. *Chem. Soc. Rev.* **2011**, *40* (11), 5242−5253.

(8) Knoops, H. C. M.; Donders, M. E.; van de Sanden, M. C. M.; Notten, P. H. L.; Kessels, W. M. M. *J. Vac. Sci. Technol., A* **2012**, *30* (1), 010801.

(9) Marichy, C.; Bechelany, M.; Pinna, N. *Adv. Mater.* **2012**, *24* (8), 1017−1032.

(10) Peng, Q.; Lewis, J. S.; Hoertz, P. G.; Glass, J. T.; Parsons, G. N. *J. Vac. Sci. Technol. A* **2012**, *30* (1), 010802.

(11) Meng, X.; Yang, X.-Q.; Sun, X. *Adv. Mater.* **2012**, *24* (27), 3589−3615.

(12) Scott, I. D.; Jung, Y. S.; Cavanagh, A. S.; Yan, Y.; Dillon, A. C.; George, S. M.; Lee, S.-H. *Nano Lett.* **2010**, *11* (2), 414−418.

(13) Jung, Y. S.; Cavanagh, A. S.; Dillon, A. C.; Groner, M. D.; George, S. M.; Lee, S.-H. *J. Electrochem. Soc.* **2010**, *157* (1), A75−A81.

(14) Woo, J. H.; Trevey, J. E.; Cavanagh, A. S.; Choi, Y. S.; Kim, S. C.; George, S. M.; Oh, K. H.; Lee, S.-H. *J. Electrochem. Soc.* **2012**, *159* (7), A1120−A1124.

(15) Zhao, J.; Wang, Y. *J. Phys. Chem. C* **2012**, *116* (22), 11867−11876.

(16) Jung, Y. S.; Cavanagh, A. S.; Yan, Y.; George, S. M.; Manthiram, A. *J. Electrochem. Soc.* **2011**, *158* (12), A1298−A1302.

(17) Zhang, X.; Belharouak, I.; Li, L.; Lei, Y.; Elam, J. W.; Nie, A.; Chen, X.; Yassar, R. S.; Axelbaum, R. L. *Adv. Energy Mater.* **2013**, DOI: 10.1002/aenm.201300269.

(18) Leung, K.; Qi, Y.; Zavadil, K. R.; Jung, Y. S.; Dillon, A. C.; Cavanagh, A. S.; Lee, S.-H.; George, S. M. *J. Am. Chem. Soc.* **2011**, *133* (37), 14741−14754.

(19) Kasavajjula, U.; Wang, C. S.; Appleby, A. J. *J. Power Sources* **2007**, *163* (2), 1003−1039.

(20) Xiao, L. F.; Cao, Y. L.; Xiao, J.; Wang, W.; Kovarik, L.; Nie, Z. M.; Liu, J. *Chem. Commun.* **2012**, *48* (27), 3321−3323.

(21) Xiao, X. C.; Lu, P.; Ahn, D. *Adv. Mater.* **2011**, *23* (34), 3911−3915.

(22) Memarzadeh Lotfabad, E.; Kalisvaart, P.; Cui, K.; Kohandehghan, A.; Kupsta, M.; Olsen, B.; Mitlin, D. *Phys. Chem. Chem. Phys.* **2013**, *15* (32), 13646−13657.

(23) Kim, S.-W.; Seo, D.-H.; Ma, X.; Ceder, G.; Kang, K. *Adv. Energy Mater.* **2012**, *2* (7), 710−721.

(24) Wang, L.; Lu, Y.; Liu, J.; Xu, M.; Cheng, J.; Zhang, D.; Goodenough, J. B. *Angew. Chem.* **2013**, *125* (7), 2018−2021.

(25) Palomares, V.; Serras, P.; Villaluenga, I.; Hueso, K. B.; Carretero-Gonzalez, J.; Rojo, T. *Energy Environ. Sci.* **2012**, *5* (3), 5884−5901.

(26) Thackeray, M. M.; Wolverton, C.; Isaacs, E. D. *Energy Environ. Sci.* **2012**, *5* (7), 7854−7863.

(27) Zhu, Y.; Han, X.; Xu, Y.; Liu, Y.; Zheng, S.; Xu, K.; Hu, L.; Wang, C. *ACS Nano* **2013**, *7* (7), 6378−6386.

(28) Chevrier, V. L.; Ceder, G. *J. Electrochem. Soc.* **2011**, *158* (9), A1011−A1014.

(29) Datta, M. K.; Epur, R.; Saha, P.; Kadakia, K.; Park, S. K.; Kuma, P. N. *J. Power Sources* **2013**, *225*, 316−322.

(30) Xu, Y.; Zhu, Y.; Liu, Y.; Wang, C. *Adv. Energy Mater.* **2013**, *3* (1), 128−133.

(31) Liu, Y.; Xu, Y.; Zhu, Y.; Culver, J. N.; Lundgren, C. A.; Xu, K.; Wang, C. *ACS Nano* **2013**, *7* (4), 3627−3634.

(32) Komaba, S.; Matsuura, Y.; Ishikawa, T.; Yabuuchi, N.; Murata, W.; Kuze, S. *Electrochem. Commun.* **2012**, *21*, 65−68.

(33) Rotole, J. A.; Sherwood, P. M. A. *Surf. Sci. Spectra* **1998**, *5* (1), 18−24.

(34) Huang, J. Y.; Zhong, L.; Wang, C. M.; Sullivan, J. P.; Xu, W.; Zhang, L. Q.; Mao, S. X.; Hudak, N. S.; Liu, X. H.; Subramanian, A.; Fan, H.; Qi, L.; Kushima, A.; Li, J. *Science* **2010**, *330* (6010), 1515−1520.

(35) Wang, J. W.; Liu, X. H.; Mao, S. X.; Huang, J. Y. *Nano Lett* **2012**, *12* (11), 5897−902.

(36) McDowell, M. T.; Lee, S. W.; Harris, J. T.; Korgel, B. A.; Wang, C.; Nix, W. D.; Cui, Y. *Nano Lett* **2013**, *13* (2), 758−64.

(37) Ghassemi, H.; Au, M.; Chen, N.; Heiden, P. A.; Yassar, R. S. *ACS Nano* **2011**, *5* (10), 7805−7811.

(38) Liu, X. H.; Zhang, L. Q.; Zhong, L.; Liu, Y.; Zheng, H.; Wang, J. W.; Cho, J.-H.; Dayeh, S. A.; Picraux, S. T.; Sullivan, J. P.; Mao, S. X.; Ye, Z. Z.; Huang, J. Y. *Nano Lett.* **2011**, *11* (6), 2251−2258.

(39) Liu, Y.; Hudak, N. S.; Huber, D. L.; Limmer, S. J.; Sullivan, J. P.; Huang, J. Y. *Nano Lett.* **2011**, *11* (10), 4188−4194.

(40) Jung, S. C.; Han, Y.-K. *J. Phys. Chem. Lett.* **2013**, *4* (16), 2681−2685.

(41) Wang, C. M.; Xu, W.; Liu, J.; Zhang, J. G.; Saraf, L. V.; Arey, B. W.; Choi, D. W.; Yang, Z. G.; Xiao, J.; Thevuthasan, S.; Baer, D. R. *Nano Lett.* **2011**, *11* (5), 1874−1880.

(42) Xu, L. P.; Kim, C.; Shukla, A. K.; Dong, A. G.; Mattox, T. M.; Milliron, D. J.; Cabana, J. *Nano Lett.* **2013**, *13* (4), 1800−1805.

(43) Kravchyk, K.; Protesescu, L.; Bodnarchuk, M. I.; Krumeich, F.; Yarema, M.; Walter, M.; Guntlin, C.; Kovalenko, M. V. *J. Am. Chem. Soc.* **2013**, *135* (11), 4199−4202.

(44) McDowell, M. T.; Woo Lee, S.; Wang, C.; Cui, Y. *Nano Energy* **2012**, *1* (3), 401−410.

(45) Kim, J. Y.; King, D. E.; Kumta, P. N.; Blomgren, G. E. *J. Electrochem. Soc.* **2000**, *147* (12), 4411−4420.

Supporting Information

Atomic-Layer-Deposition Oxide Nano-Glue for Sodium Ion Batteries

Xiaogang Han[1,(a)], Yang Liu[2,(a)], Zheng Jia[3, (a)], Yu-Chen Chen[1], Jiayu Wan[1], Nicholas Weadock[1], Karen J. Gaskell[4], Teng Li[3,*], Liangbing Hu[1,*]

1. Department of Materials Science and Engineering, University of Maryland, College Park, MD 20742, US
2. Center for Integrated Nanotechnologies (CINT), Sandia National Laboratories, Albuquerque, New Mexico 87185, US
3. Department of Mechanical Engineering, University of Maryland, College Park, MD 20742, US
4. Department of Chemistry and Biochemistry, University of Maryland, College Park, MD 20742, US

Corresponding Authors: binghu@umd.edu; LiT@umd.edu

Methods

Synthesis of Al₂O₃/SnNPs@CNF. The hybrid nanostructure Al_2O_3/SnNPs@CNF is synthesized with three steps: electrospinning, carbonization, and ALD treatment. The $SnCl_2$ composite fibers are prepared firstly by electrospinning the precursor solution of 0.4 M $SnCl_2 \cdot 2H_2O$, 0.2 M citrate acid, and 10 wt.% PAN in DMF. The obtained electrospun mat was then stabilized in air at 240 °C for 3 hours, and carbonized in Ar/H_2 (5% H_2, v/v) at 650 °C for 5 hours with a heat rate of 2 °C/min. The $SnCl_2$ decomposed to form liquid Sn (m.p. 232 °C) which drained out of the carbon fiber. Due to the liquid Sn surface tension, regular spherical Sn particles formed on the fiber walls (SnNPs@CNF) before condensation when cooling down. The resultant SnNPs@CNF mat was placed into an atomic layer deposition system (Beneq TFS 500) for Al_2O_3 deposition. High-purity nitrogen at 150 °C was used as carrier gas for the whole process. To reinforce the robustness and preserve the conductivity for the structure as much as possible, 60 cycles of ALD-Al_2O_3 were performed. Each cycle included alternating flows of trimethylaluminum (TMA, 4 sec, Al precursor) and water (4 sec, oxidant) separated by flows of pure nitrogen gas (4 and 10 sec, respectively, carrier and cleaning gas). The thin layer of Al_2O_3 was estimated according to a control with atomic force microscopy (AFM).

Characterization. SEM (Scanning Electron Microscopy) was performed with a Hitachi SU-70 analytical scanning electron microscope with an energy-dispersive X-ray detector (Bruker silicon drift detector). Micro-Raman analysis was performed with a Horiba Yvon LabRam ARAMIS confocal Raman microscope with a helium neon laser excitation source (632.8 nm), and the crystal structure analysis was performed with powder X-ray diffraction (XRD) on D8 Advanced with LynxEye and SolX (Bruker AXS, WI, USA) using a Cu Kα

radiation source operated at 40 kV and 40 mA. XPS data were collected on a Kratos Axis 165 x-ray photoelectron spectrometer operating in hybrid mode using monochromatic Al Kα x-rays (1486.7 eV). Survey spectra and high resolution spectra were collected with pass energies of 160 eV and 20 eV respectively. Charge neutralization was required to minimize surface charging. The thermogravimetric analysis (TGA) was performed on the TGA equipment (CAHN TG 2131, USA) and heated from room temperature to 800 °C in air with a heating rate of 5 °C/min and the gas flow rate of 2 mL/min.

In situ TEM electrochemical sodiation/desodiation experiments. Our experiments were conducted with a FEI Tecnai F30 transmission electron microscope (TEM) at room temperature. For the setup of the half-cell (Figure 3a), the Al_2O_3/SnNPs@CNF structures were glued using conductive epoxy on the Al rod, serving as the working electrode. A piece of Na metal was scratched off and stuck to a W rod inside a glove box filled with dry helium (H_2O and O_2 concentration below 0.6 ppm), serving as the counter electrode. The two electrodes were mounted onto the Nanofactory TEM-scaning tunneling microscopy (STM) holder in the glovebox and further sealed in a plastic bag filled with dry helium. During the transfer of the TEM holder into the TEM column, the Na metal was exposed to air for about 2 s, resulting in formation of a surface Na_2O and NaOH mixed layer, which can serve as the solid electrolyte for Na ion transport. Inside the TEM, with the help of the piezo-manipulator, the Na electrode can be driven to contact the selected carbon fiber with the solid electrolyte in between, which constructs a half cell of a nano-sodium ion battery _in situ_. Typical potentials of -2 V to -6V were applied to the Al_2O_3/SnNPs@CNF anode to initiate the sodiation, and +2 V to +6 V were used for desodiation. Since the sodiated Sn particle is very sensitive to the electron beam, in order to avoid the accumulative electron

dose effects on the subsequent cycles in collecting EFTEM mapping, different Sn particles were used to collect mapping information.

Electrochemical measurement in coin-cells. In the coin cells (CR2032), sodium metal disks are used as both counter and reference electrodes for the half cells, with 1 M NaPF$_6$ in EC:DEC (1:1, m/m) electrolyte and the microporous membrane separator (Celgard 3501). The Al$_2$O$_3$/SnNPs@CNF mat was used as cathode working electrode directly without binders or extra conductive materials added. The half cells were assembled in an argon-filled glovebox (oxygen content $\leq$ 0.1 ppm, water content $\leq$ 0.5 ppm). The half cells were tested at room temperature (23 -25 ^{o}C) using a BioLogic battery tester. Typically, the voltage is 0.02 to 1.5 V with a current density of 84.7 mA/g (0.1 C, 1C=847 mA/g).

Ex situ **SEM imaging.** Scanning electron microscope (SEM) and energy-dispersive X-ray analysis (EDX) characterizations were performed with a Hitachi SU-70 SEM. No conductive coatings were required to image the samples. For *ex situ* SEM, the corresponding anode samples (Al$_2$O$_3$/SnNPs@CNF or SnNPs@CNF) were removed from the coin cells, dipped and washed with acetone and acetonitrile several times to remove any residual electrolyte.

Simulation method and parameters

In the chemomechanical simulation, the SnNP electrode is initially pristine and subjected to a constant sodium flux during sodiation and desodiation. Taking advantage of axisymmetric condition, only half of the cross section of the SnNP/CNF structure is simulated in order to reduce the computational cost. An elastic-perfectly plastic constitutive law with a Young's Modulus of 30GPa and a yielding stress σ_Y of 2GPa is assumed for sodiated Sn. CNF and Na-Al-O are taken to be linear elastic materials with

Young's Moduli of 200GPa and 100GPa respectively. All interfaces including the CNF/ALD interface, CNF/Sn interface, and Sn/ALD interface are all simulated by cohesive surface behavior. The interfacial toughness of the CNF/ALD interface and Sn/ALD interface is assumed to be $20J/m^2$ and the interfacial toughness of Sn/CNF interface is taken to be $0.5J/m^2$. Charging rate is C/5.
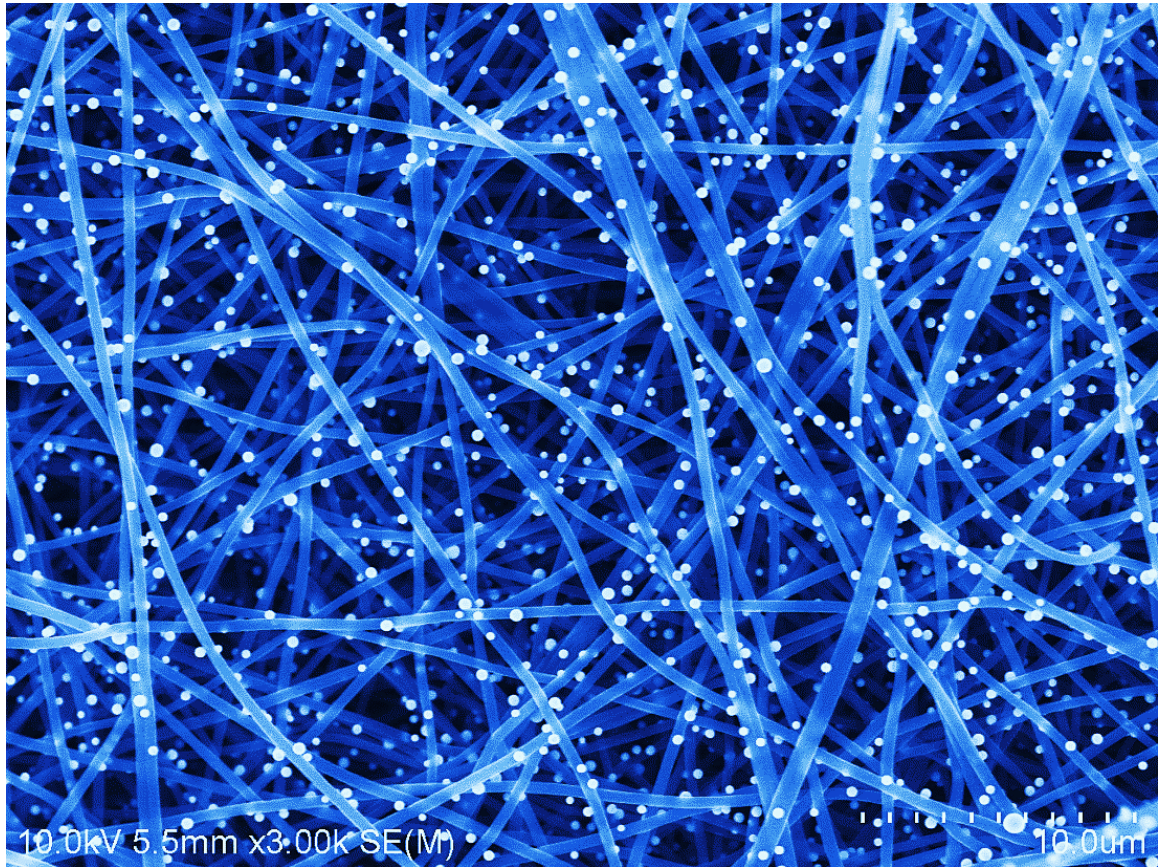
Supplementary Figures

Figure S1. SEM image of the as-made Al_2O_3/SnNPs@CNF. The image was colored in Microsoft® Powerpoint.
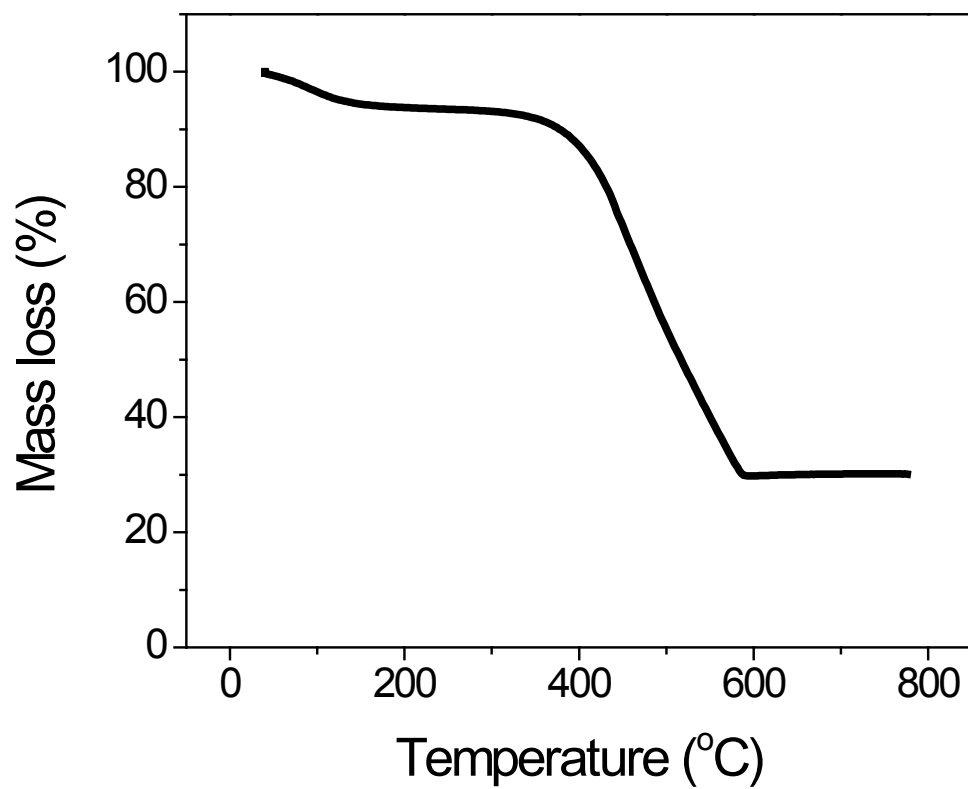
Figure S2. Thermogravimetric analysis (TGA) of the as-made Al2O3/SnNPs@CNF. The TGA was performed on the TGA equipment (*CAHN TG 2131, USA*) in air with a heating rate of 5 °C/min.
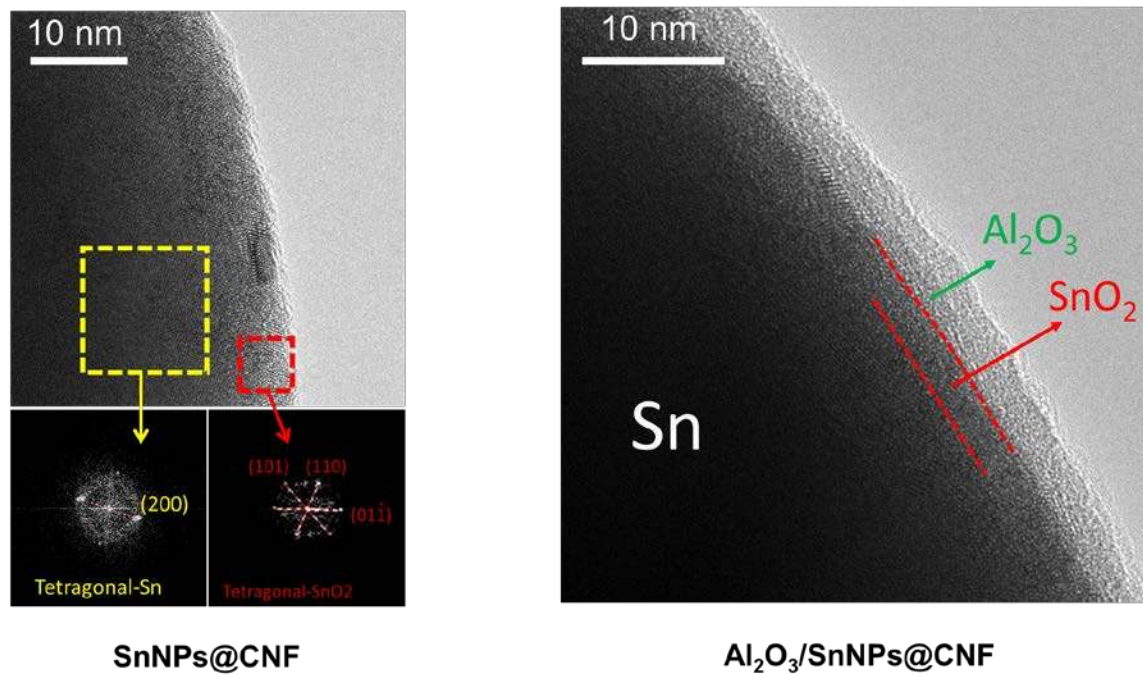
Figure S3. HRTEM images and FFT patterns for the hybrid structure without and with ALD coating. Left: HRTEM image and FFT patterns of SnNPs@CNF show Sn metal for inner and SnO_2 for outer surface. Right: after ALD treatment, HRTEM show layered structure for the surface of SnNPs: Al_2O_3, SnO_2, and Sn sequentially from outside to inside.
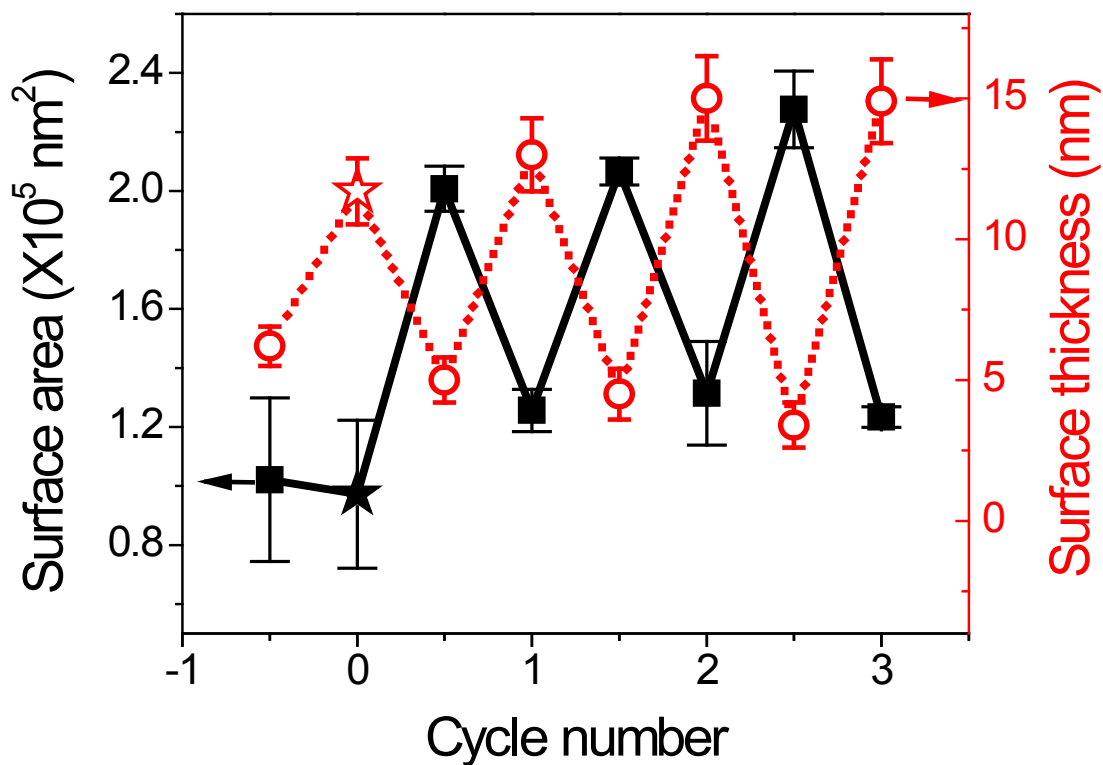
Figure S4. Inner surface area and thickness change of ALD-Al$_2$O$_3$ coating layer upon *in situ* TEM electrochemical sodiation/desodiation cycles. The inner surface area change is calculated based on the SnNP core volume expansion in corresponding cycles.
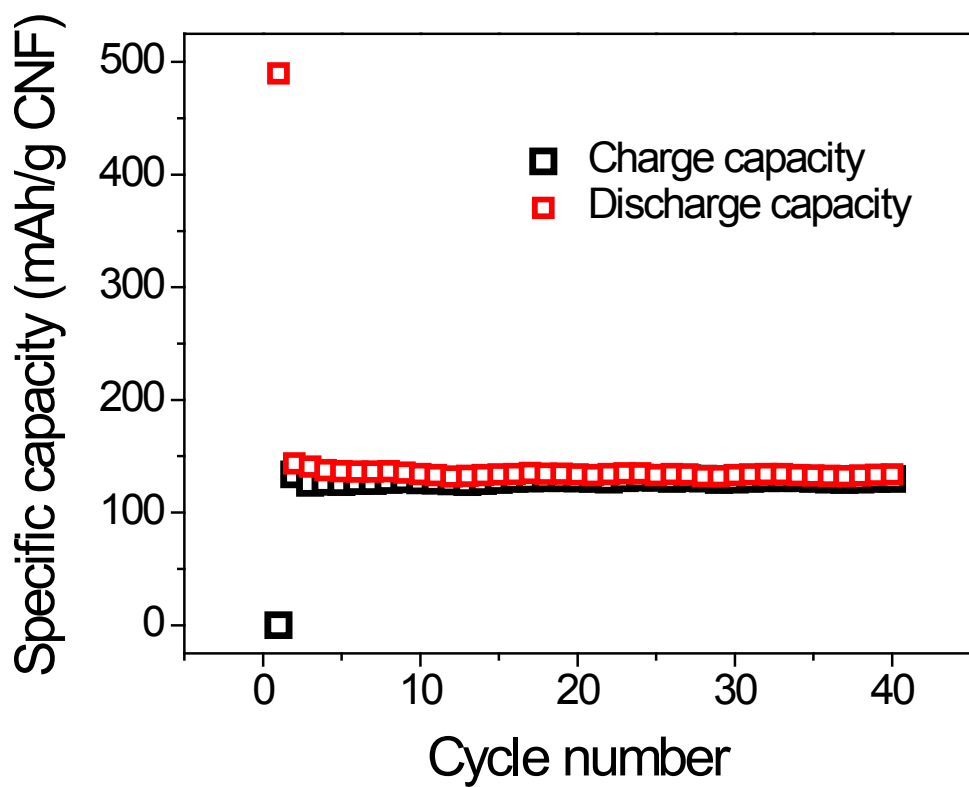
Figure S5. Capacity contribution of the carbon nanofibers. Specific capacity of the carbon nanofibers (CNF) as the only anodes in sodium ion batteries.
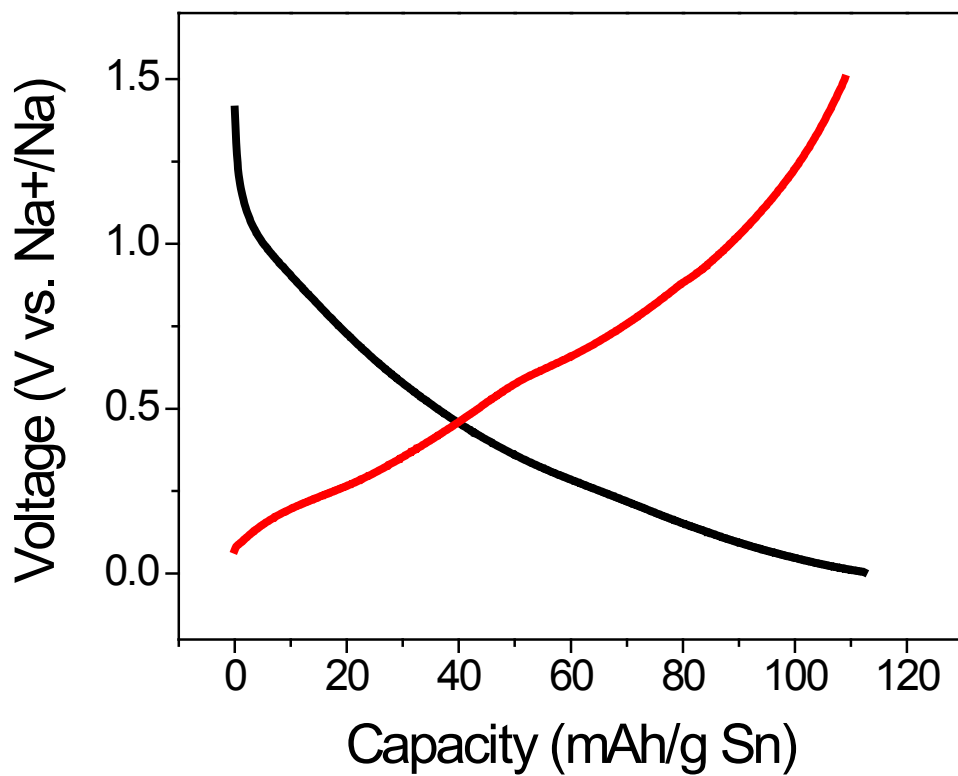
Figure S6. Voltage profile of the control SnNPs@CNF anode at the 40th cycle. The specific capacity is calculated based on the Sn mass less contribution from the carbon (CNF).
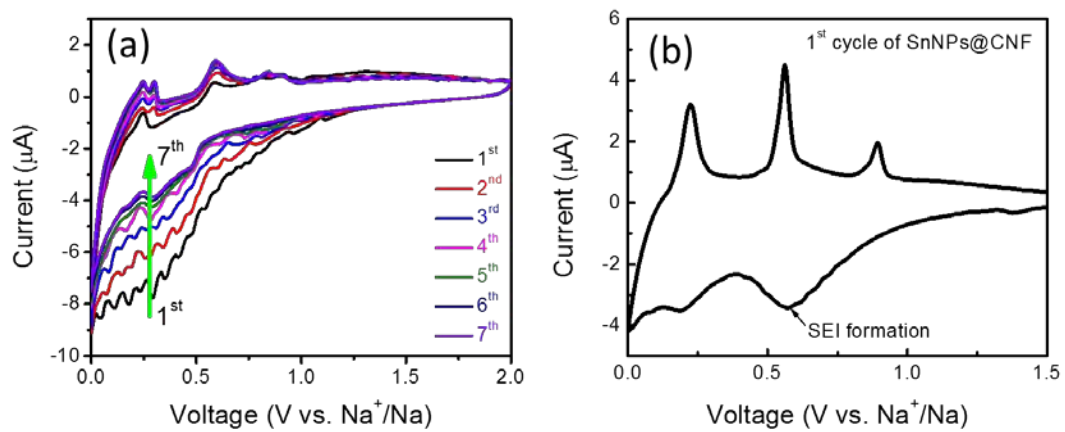
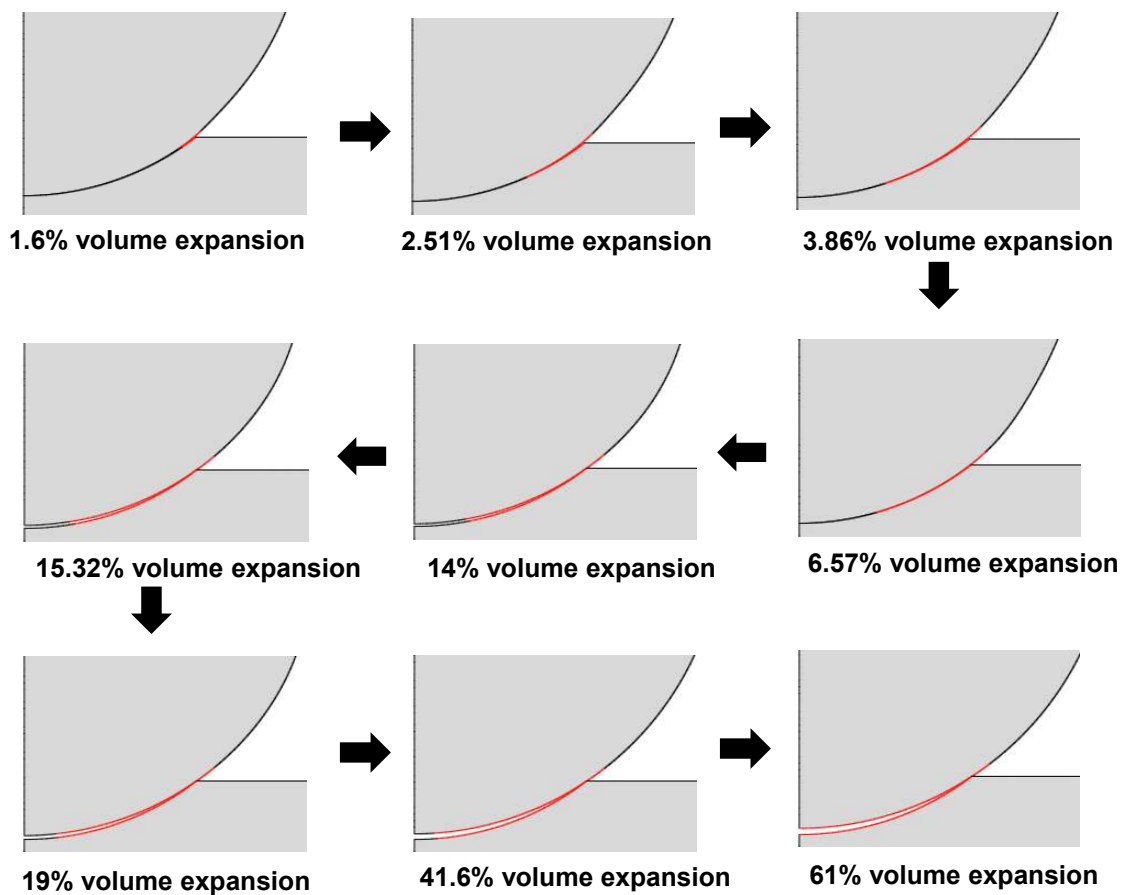**Figure S7.** Cyclic voltammetry of the anode Al_2O_3/SnNPs@CNF (a) and SnNPs@CNF (b).

Figure S8. Simulated debonding process of bare Sn particle on CNF. Delamination propagates along the interface as sodiation proceeds. Finally, the Sn particle is totally debonded from the underlying CNF. Red color represents delamination while black represents regions still in contact.
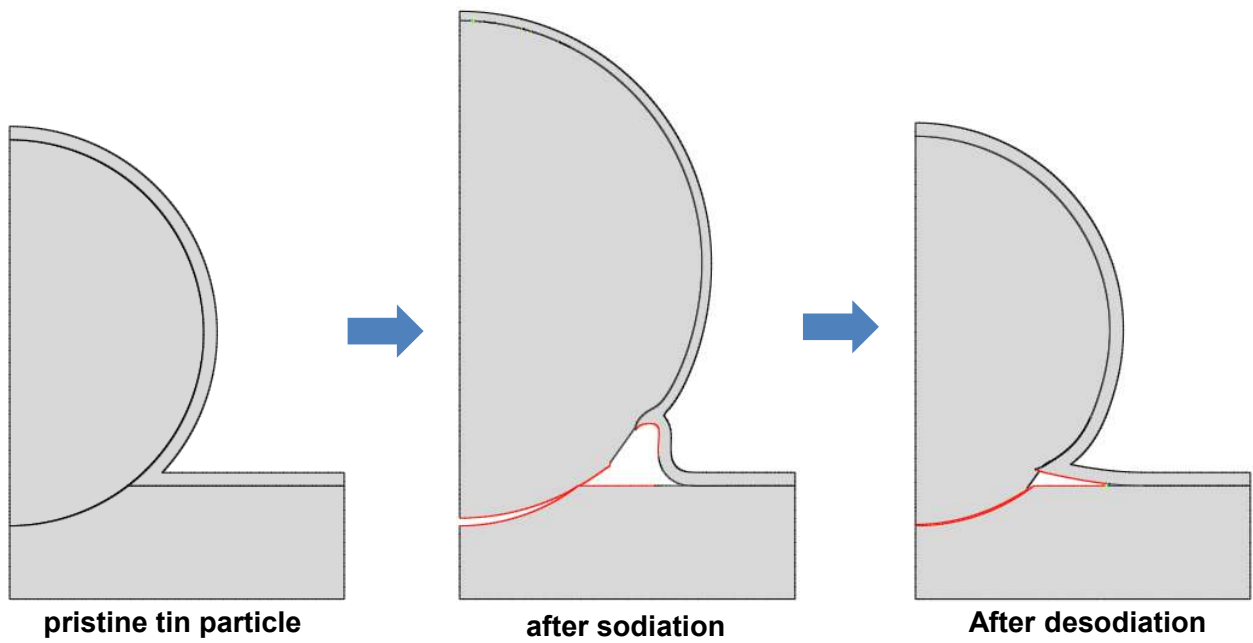
pristine tin particle **after sodiation** **After desodiation**

Figure S9. Shape change of ALD-coated Sn particle after sodiation and desodiation. The large volume change of the Sn particle detaches the Sn particle from the underlying CNF. However, the tough and ductile Na-Al-O layer holds the particle in its original position.
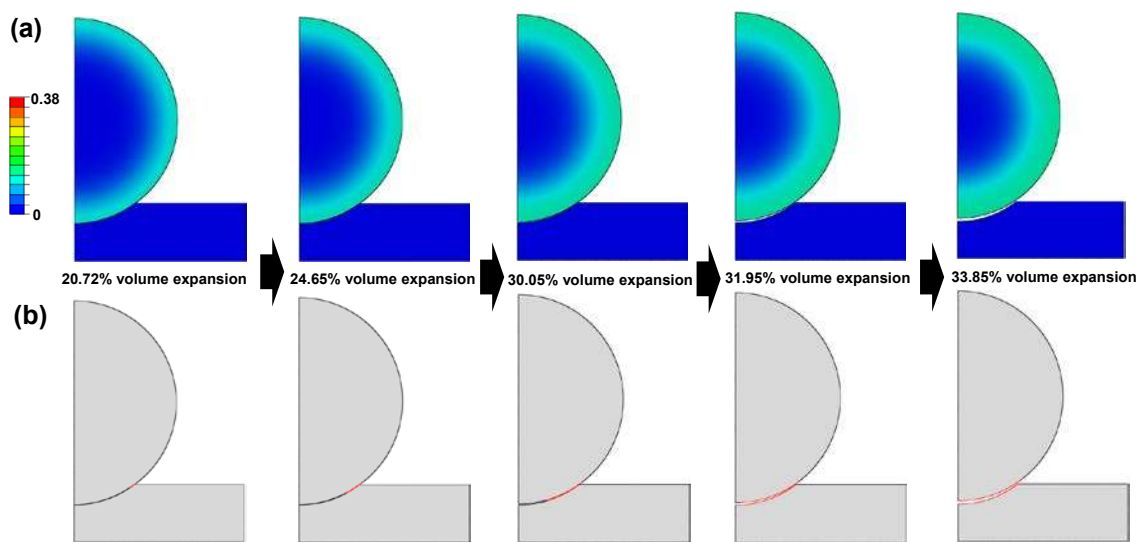
Figure S10. Simulated debonding process of bare Sn particle immersed in electrolyte. Na inserts into a Sn particle through the whole outer surface, forming an unsodiated core wrapped by a sodiated Sn shell. A similar delamination process to that presented in Figure S5 is shown. The Sn particle is totally debonded from the underlying CNF when the volume expansion reaches 33.85%. Red color at the interface represents delamination while black color represents regions still in contact.
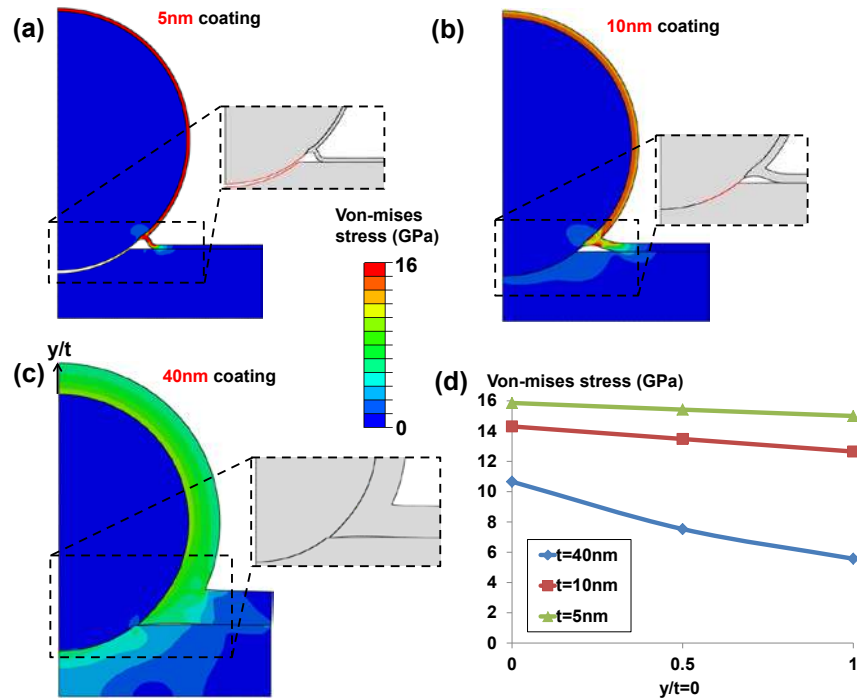
Figure S11. Delamination status at SnNPs/CNF interface at 56% volume expansion for 5nm (a), 10nm (b) and 40nm (c) ALD AL_2O_3 coating. Von-mises stress distribution along thickness direction of ALD coating (d).
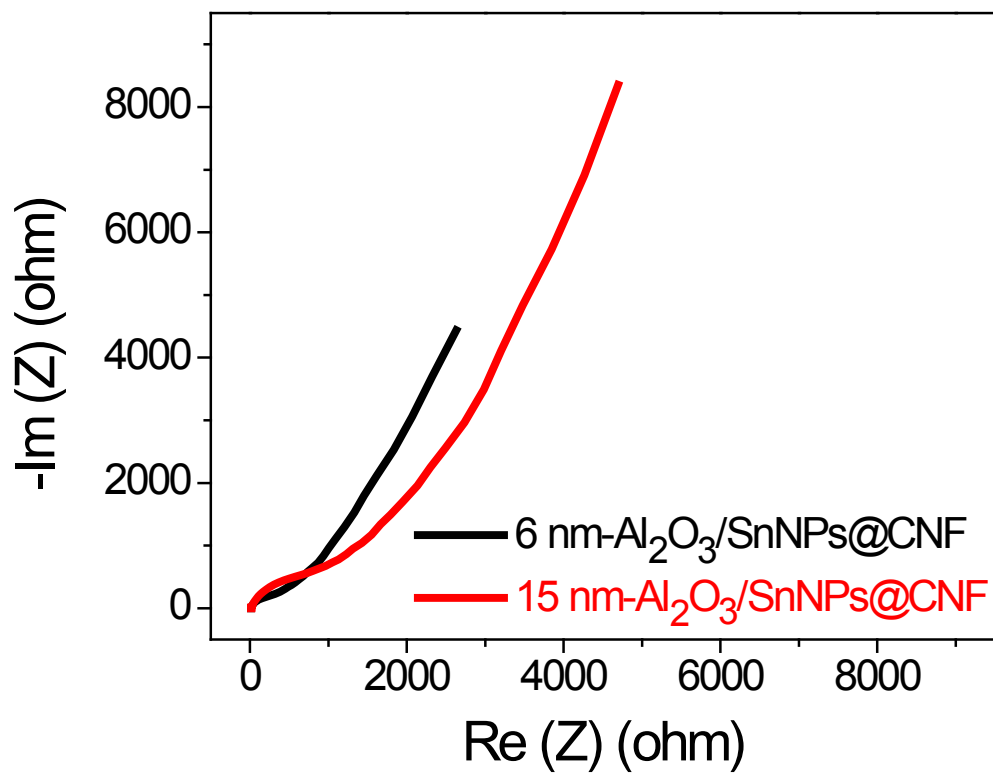
Figure S12. The electrochemistry impedance spectra of SnNPs@CNF with 6 nm and 15 nm ALD-Al$_2$O$_3$ coating, respectively.

Supplementary Table

Table S1. Relative atomic percentage composition calculated from XPS for SnNPs@CNF and Al_2O_3/SnNPs@CNF samples. The Al_2O_3 layer is shown to sit on top of the SnNPs and CNF as evidenced by the attenuation of the Sn signal by ~ 25 times, and the C signal in the presence of the Al_2O_3 ALD layer.

Anode Material	Relative Elemental Percentage Composition			
	C	Al	Sn	O
SnNPs@CNF	90.7	-	1.6	7.7
Al_2O_3/SnNPs@CNF	16.3	31.0	0.1	52.6

Supplementary Movies

Movie M1. *In situ* TEM movie of surface sodiation of Al_2O_3/SnNPs@CNF.

Movies M2-M7. *In situ* TEM movies of three cycles of sodiation/desodiation of Al_2O_3/SnNPs@CNF:

- **Movie M2.** First sodiation

- **Movie M3.** First desodiation

- **Movie M4.** Second sodiation

- **Movie M5.** Second desodiation

- **Movie M6.** Third sodiation

- **Movie M7.** Third desodiation

Movies M8-M11 | Chemomechanical modeling results:

- **Movie M8.** Na distribution in bare Sn particle

- **Movie M9.** Debonding process of bare Sn particle

- **Movie M10.** Na distribution in ALD-coated Sn particle

- **Movie M11.** Debonding process of ALD-coated Sn particle